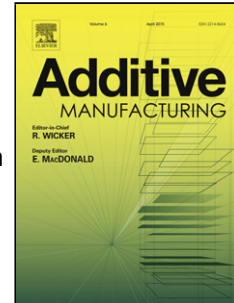


# Journal Pre-proof

Killer notches: the effect of as-built surface roughness on fatigue failure in AlSi10Mg produced by laser powder bed fusion

A. du Plessis, S. Beretta



PII: S2214-8604(20)30796-X

DOI: <https://doi.org/10.1016/j.addma.2020.101424>

Reference: ADDMA 101424

To appear in: *Additive Manufacturing*

Received Date: 20 March 2020

Revised Date: 23 June 2020

Accepted Date: 26 June 2020

Please cite this article as: du Plessis A, Beretta S, Killer notches: the effect of as-built surface roughness on fatigue failure in AlSi10Mg produced by laser powder bed fusion, *Additive Manufacturing* (2020), doi: <https://doi.org/10.1016/j.addma.2020.101424>

This is a PDF file of an article that has undergone enhancements after acceptance, such as the addition of a cover page and metadata, and formatting for readability, but it is not yet the definitive version of record. This version will undergo additional copyediting, typesetting and review before it is published in its final form, but we are providing this version to give early visibility of the article. Please note that, during the production process, errors may be discovered which could affect the content, and all legal disclaimers that apply to the journal pertain.

© 2020 Published by Elsevier.

## Killer notches: the effect of as-built surface roughness on fatigue failure in AISi10Mg produced by laser powder bed fusion

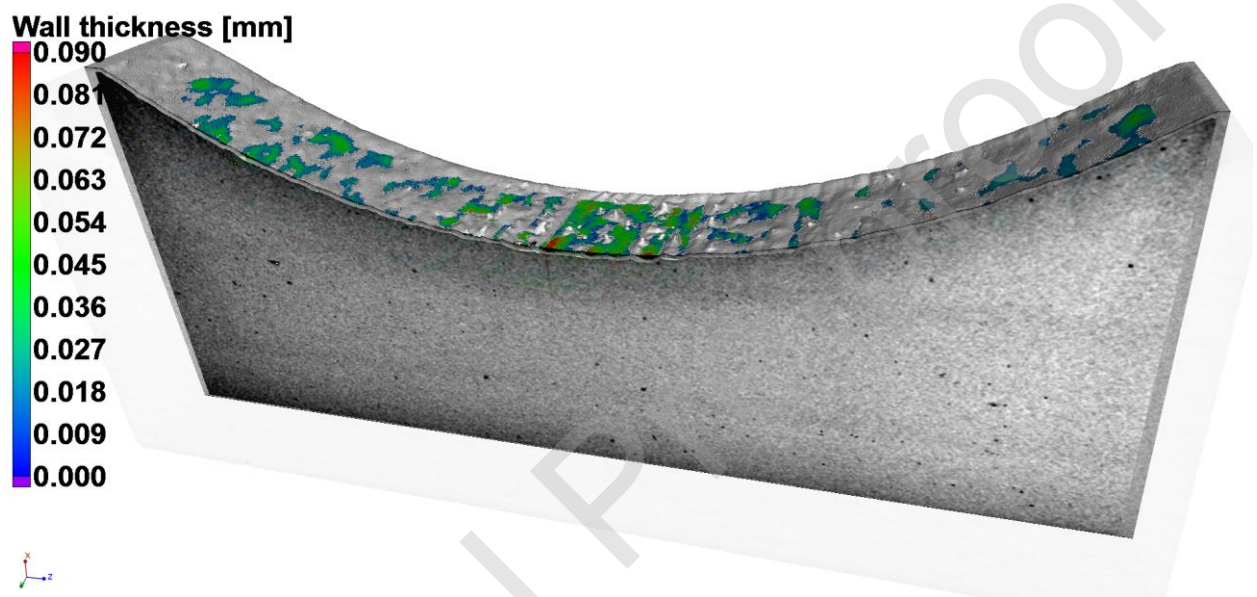
A. du Plessis<sup>1,2</sup>, S. Beretta<sup>3</sup>

<sup>1</sup> Research group 3DInnovation, Stellenbosch University, Stellenbosch 7602, South Africa

<sup>2</sup> Department of Mechanical Engineering, Nelson Mandela University, Port Elizabeth 6001, South Africa

<sup>3</sup> Politecnico di Milano, Via La Masa 1, 20156, Milan, Italy

Graphical Abstract



**Abstract**

Additive manufacturing allows the production of complex components for critical applications such as in the aerospace industry. Laser powder bed fusion is the most widely used form of additive manufacturing and good progress has been made in improved material quality in recent years. Despite the progress, fatigue properties are sometimes still problematic and this requires further investigation. The fatigue properties of additively manufactured metals depend on a variety of factors including surface roughness, microstructure, porosity and residual stress, amongst others. In this work the role of surface roughness in particular is evaluated using micro computed tomography (microCT) scans before and after fatigue tests. The crack locations are identified in scans after fatigue testing and correlated with surface features prior to fatigue tests by careful alignment of CT images. In this way notches on the surface which act as “killer notches” are measured and compared with other defects (both roughness notches and pores) in the vicinity. Direct evidence is thereby provided for specific features acting as killer defects, studied with varying surface topographies depending on build orientation. A statistical analysis using stress intensity factor and fatigue test results of the same samples directly validate the effect of the notches, in comparison to other similar notches across the sample. This is the first notch-based surface roughness evaluation method reported using X-ray tomography, showing promise as analytical methodology. In addition, the experimental campaign shows for the first time a direct correlation of fatigue strength with surface roughness using different typical as-built surfaces. This work lays the foundation for improved non-destructive testing, predictive modelling and overall improvement and management of the performance of additively manufactured parts based on surface features and surface characterization.

Keywords: metal additive manufacturing; laser powder bed fusion; surface roughness; X-ray tomography; fatigue crack; killer notches

## 1. Introduction

Metal additive manufacturing (AM) is a rapidly growing production method for highly critical components in various industries. The most widely used AM method is laser powder bed fusion (LPBF) which allows high quality parts to be produced by selectively melting layers of powder using a fast moving, high-power laser beam across a tightly packed powder bed [1,2]. Various alloys can be produced by LPBF including popular aerospace alloys such as Ti6Al4V & AlSi10Mg, with excellent material properties reported in various studies [3,4]. However, some problems can arise which cause scatter in fatigue properties [5,6]. This variable fatigue performance can be caused by a number of underlying problems which can be difficult to identify due to the complexity of the LPBF process.

The most well-known issues which have been correlated with poor fatigue performance are porosity, surface roughness, residual stress and microstructure, all of which can contribute to the obtained properties in different relative amounts depending on the alloy and other details of the production (e.g. process parameters, build orientation, etc.). In general, the effects of surface defects, microporosity and inclusions in metals on fatigue performance is recognized and understood, as reviewed in [7–10]. Much work has focused on the effects of pores on the mechanical performance of additively manufactured parts, as summarized in [11,12]. It is also understood that there is a competition between porosity, surface roughness, residual stress and microstructure, which is interrelated in complex relationships and may depend on part geometry and size due to differences in thermal history [13].

An improved understanding of the effects of all types of defects in additive manufacturing will assist in efforts to predict the performance of additively manufactured materials, which all forms part of the materials qualification needs for these materials for high criticality applications [6]. Towards this aim, a defect-based modelling approach for internal pores has been used with great success [12,14,15]. This was also demonstrated for surface and subsurface pores in [16]. In [15] the authors clearly demonstrated, by the detection through computed tomography (CT) scan of all the defects present in specimens, that the critical defects were the ones with the largest stress intensity factor (SIF), thus supporting the adoption of “extreme value” concepts for estimating the maximum size of defects for fatigue assessment [12] and for comparing the “quality” of different treatments [17,18].

While these approaches are useful, it was also demonstrated in [19] that there is a strong interaction between local surface features and pores, which cannot be ignored and may have a higher influence for example when a pore is located at the surface. The fact that (in general) most crack initiation occurs on surface or near-surface pores highlights the importance of surface quality for improving fatigue properties. Many studies make use of post-process machining or treatment of the surface for improved surface quality, for example by laser shock peening [20,21]. However, the major advantage of additive manufacturing is the complexity of design. When this complexity is utilized, for example in topology optimized or latticed structures [22], many surfaces may not be accessible for processing, and the as-built surface is of particular importance.

As-built additively manufactured surfaces are well known to be relatively rough and to depend on build angle and process parameters [23]. It has been demonstrated that cracks initiate at sharp micro-notches on the surface of as-built specimens (as clearly shown by Nicoletto [24] comparing the same material with different processes). Due to this, variations in fatigue strength depending on the build orientation and hence surface roughness have been reported [25]. Recent work showed how different shapes of intentionally designed notches affect mechanical performance and crack initiation, showing that there is a competition between global notches (designed) and local notches (due to as-built surface) [26]. The fatigue strength dependence on

notch depth has been studied in detail in Ti6Al4V [27], revealing that the failures are driven by the size of the largest defect in the vicinity of the notch.

X-ray tomography has been used with great success to provide insights into additively manufactured materials, also for viewing of fatigue crack locations [28–30]. Recently the detailed analysis of thin struts manufactured in Ti6Al4V combining CT-scan and scanning electron microscopy (SEM) showed that the effect of surface features responsible for fatigue failures could be modelled by Kitagawa-Takahashi diagram [14,16,31]. However, a systematic study about the reasons why failure occurs in some critical surface features and their behaviour for different surface qualities is still lacking.

This study is of primary importance for two different reasons: accurate assessment for predictive modelling and general rating of surface quality. As for the modelling and assessment, there are different approaches for numerical modelling surface effects (in terms of fatigue stress concentration [32–36] or cracks [19,37–42]), but these approaches were applied thus far for conservative predictions without a ‘sample by sample’ verification. As for the measurement of surface quality, the different approaches for fatigue modelling use generalized roughness parameters to describe the surface quality, but undoubtedly the concept of notch stress concentration is only related to “valleys” and depressions in the profile. This was clearly demonstrated by Gockel [43], who showed that the  $R_v$  parameter is the roughness parameter having the strongest correlation with fatigue life.

In the work reported here, a series of LPBF samples were produced at different build orientations in AlSi10Mg, in order to intentionally induce differences in their surface roughness and topography. These were subsequently subjected to high resolution microCT scans before and after 3-point bending fatigue tests. This was done with the aim to reveal the location of crack initiation relative to surface features and identify the critical features or “killer notches” in each case. Selected cases are individually discussed and S:N curves presented, providing the first direct evidence of the effects of specific as-built surface notches on fatigue performance. The analysis of the competition of the different surface features detected on each sample was carried out calculating a prospective SIF, i.e. treating the surface features as cracks. The reasons for the choice of this index are: i) the success of defects/cracks concepts [7] in describing in a unified concept both internal defects and surface asperities; ii) the connection of these concepts to new ways for measuring and sampling the defects [44,45] that also led to implementations into standards (i.e. ASTM standard E2283-03 [46]).

The paper is organized as follows: Section 2 describes the set-up and how the analyses were carried out; Section 3 deals with a detailed description of the results for chosen samples of different series; Section 4 presents and discusses the summary of results; Section 5 concludes the paper.

## 2. Experiments

This work makes use of 5 sample types/series – the same geometry was manufactured in different build orientations with between 3-5 replicates of each build orientation available. In all cases there are rough as-built surfaces in the AlSi10Mg samples as is typical for LPBF, but the roughness varies as does the amount of internal pores in the different build orientations. In addition to these differences, there are also differences in microstructure and residual stress. Some of these results were reported in a recent paper focusing on the fatigue performance [47]. All samples were produced for 3-point bend fatigue test with length of 60 mm and curvature of 20 mm, and were machined by 0.25 mm on the top and bottom surfaces in order to have a good parallelism of the surfaces for the contact with 3-P bending test rollers. The net minimum section of the specimens is 6 x 6 mm<sup>2</sup> (see Figure 1.a)

## 2.1 Additive manufacturing and sample preparation

The fatigue test samples were manufactured using a SLM 280HL v1.0 system equipped with 2x400W Yttrium fiber lasers that work in parallel in a build chamber of 280x280x350 mm<sup>3</sup> (SLM Solutions Group AG). During the manufacturing process, the chamber was flooded with argon to reduce the oxygen content below 0.2% and the platform was heated to 150 °C. The printing parameters were set to: beam power 350 W, hatch distance  $h = 0.13$  mm and scan speed  $v = 1650$  mm/s. A layer thickness of 50  $\mu\text{m}$  was used resulting in a volumetric energy density  $F = 32.63$  J/mm<sup>3</sup>. The scan strategy is stripes which rotate each layer by 67° and the scanning order is two contours, followed by the hatch scanning. AlSi10Mg Powder produced by ECKA granules were characterized by a mean size of 37  $\mu\text{m}$ ,  $D_{10} = 21$   $\mu\text{m}$  and  $D_{90} = 65$   $\mu\text{m}$  and a flowability of 80 s/50g. The tensile properties of the specimens (for the three orientations) were tested on machined specimens with a diameter of 3 mm and they are reported in Table 1 [47]. The results show that there is not a significant anisotropy.

It is well known from the literature that the orientation of a surface with respect to the platform determines its roughness [1]. Usually down-facing surfaces are roughest (as also shown here), with upwards facing surfaces the smoothest, for ideal flat surfaces. However, in this case there is a curvature of the surface which contributes to the complex roughness profiles. In this case the upwards facing surfaces are also reasonably rough, possibly due to stair-stepping effect on the curvature. The smoothest surfaces in this work are the side-facing surfaces. The roughness values for the five orientations were measured along the longitudinal direction of a number of 10 specimens per series, along 3 lines following the ASTM D7127 – 17 [48] with a Mahr Perthometer PRK stylus. Results are reported in Table 2 in terms of average values for the different series (further details in [47]).

The residual stress due to the manufacturing process was investigated by X-ray diffraction using the AST X-Stress 3000 portable X-ray diffractometer (CrK $\alpha$  radiation ( $\lambda_{K\alpha 1} = 2.2898$  Å)), using the  $\sin^2(\psi)$  method. The measurements were carried out along the Z-direction of the specimen. The results in terms of the average longitudinal stress (z-direction in Fig. 1.a), measured on two specimens per series, at a depth of 100 micron after electro-polishing step by step material removal on a circular area with a diameter of 0.5 cm<sup>2</sup>, are reported in Table 2 (further details in [47]).

As expected, the residual stresses vary with build orientation due to differences in thermal histories [1,49,50]. It would be expected that samples of types A and B which have direct bulk connection to the baseplate (see Figure 1) have faster cooling and hence lower residual stresses, as confirmed by the low compressive stresses measured. The sample type C without any supports built in vertical orientation has the highest tensile residual stress while samples D and E have supports which do not effectively transfer heat therefore moderate residual stresses are found.

## 2.2 Fatigue testing

The three-point bending tests were performed at a stress ratio  $R=0.1$  on an Instron Electroplus E10000 machine equipped with a 10 kN load cell, with a frequency of approximately 40 Hz, the set-up is reported in Figure 2(a). A 10% reduction in elastic dynamic stiffness was considered as a failure condition, while tests were suspended as run-outs at  $5 \times 10^6$  cycles [47].

The stress distribution for the three point bending specimen was obtained by FE elastic analysis with ABAQUS/CAE 2017 adopting quadratic hexahedral elements with a dimension of the notch root of 200 microns. The top roller was modelled with surface-to-surface contact with the specimen, that was simply supported on two rows of nodes corresponding to the contact region

of the bottom rollers. The so-obtained stress distribution remains almost constant over the width of the specimen and the stress distribution in the middle section (that was used for the SIF calculation at the tip of cavities detected by CT-scan) is reported in Figure 2(b) [51].

The reference S-N diagrams for the different test series (in terms of local stress at the failure location per each specimen) are reported in Figure 3, where the specimens here investigated are highlighted with red circles. The S-N diagrams were determined by calculating the effective local stress at the failure location per each specimens and the data were interpolated by least squares method with an equation of the type  $\log N = A + B \log(\Delta S)$ , obtaining the mean line and the 95% scatter band according to ASTM E739 [52], while the fatigue limits -  $\Delta S_{lim}$ - were calculated Dixon's formulas to the short staircase sequences [53].

The fatigue limits for the different series are reported in Table 3. As a reference, the fatigue limit of machined specs (orientations  $0^\circ$ - $90^\circ$ - $135^\circ$ ) is in the range 165-180 MPa, with pores in a size range of 20-30 micron at the fracture origin [47]. These values are very close to results by Brandl [54] for AlSi10Mg machined specs and they are also consistent with Mower's data [55] for a wrought 6061 alloy ( $\Delta S_{lim} = 210$  MPa at  $R = 0.1$ ).

The results in Figure 2 and Table 3 clearly show a strong dependence of fatigue limit on specimen orientation, as a result of the rough surface and the significant residual stresses, as acknowledged by the recent results by Nicoletto [56]. The effect of the residual stresses can be clearly seen comparing series B, C and E that have different fatigue properties even if their roughness parameters are very similar. For a detailed analysis the reader should refer to [47].

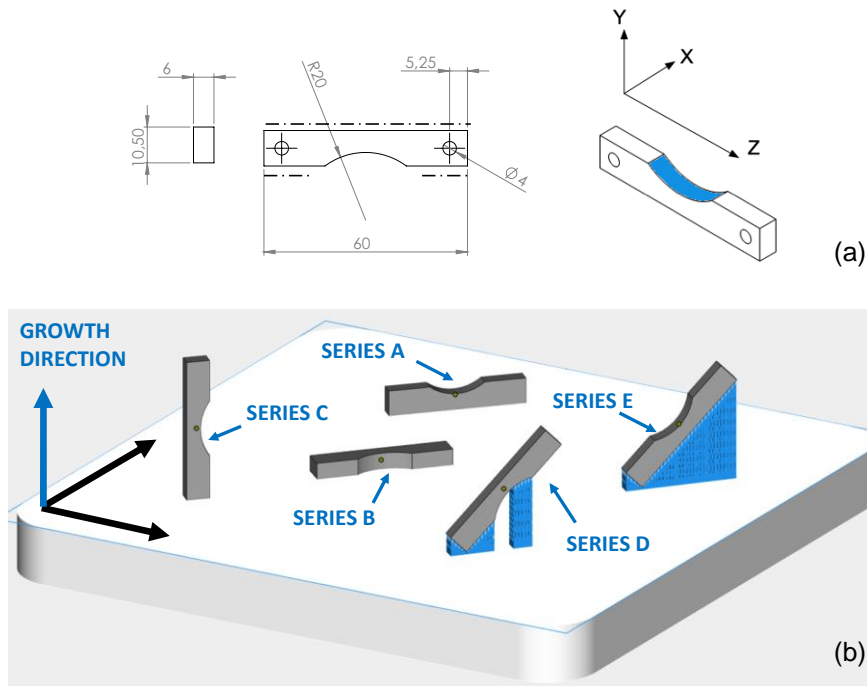


Figure 1: Details of the specimens investigated: a) shape of the specimens (the “as-built” surface of interest is the blue one, surfaces with dash-dotted line are the ones machined) ; b) Build orientations showing locations of supports, for sample series A-E.

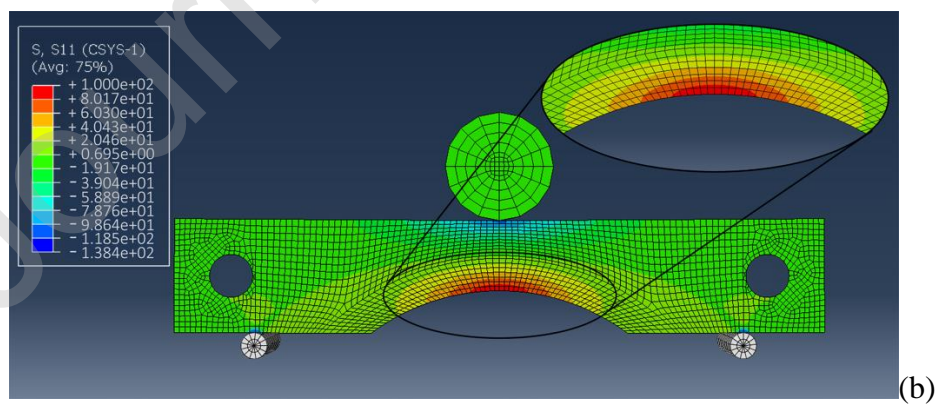
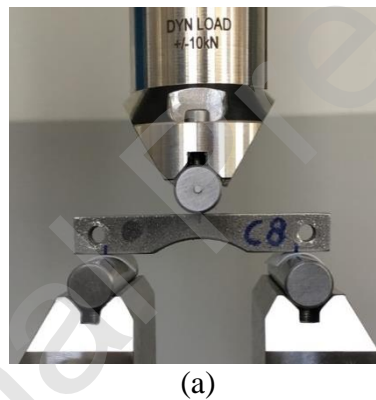


Figure 2: Details of fatigue tests: a) 3PB test setup; b) FE results of circumferential stress along the specimen (view on midsection; circumferential stresses for a cylindrical reference system located along curvature axis of the lower part) subjected to three-point bending [51].



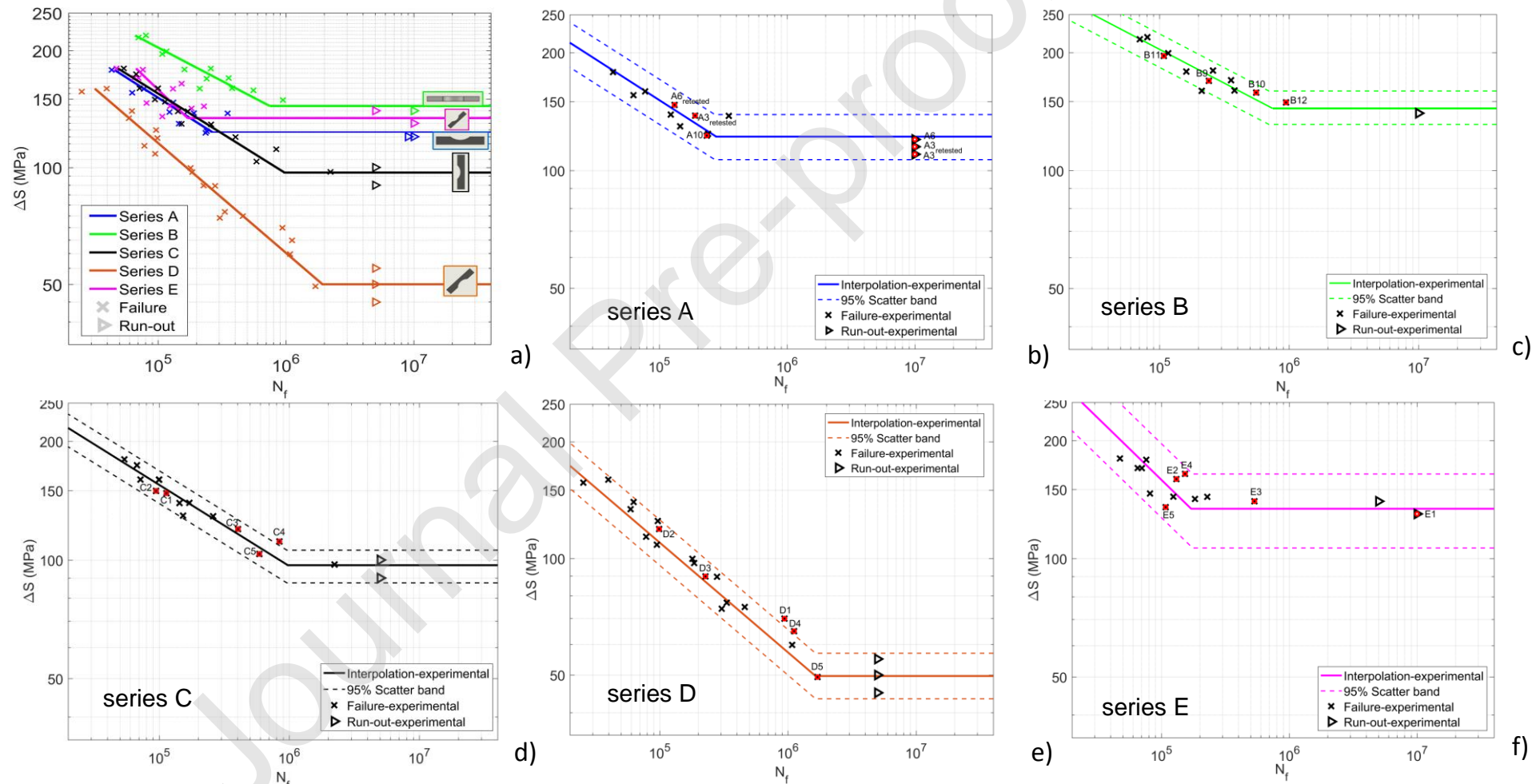


Figure 3: Results of the fatigue tests: a) reference S-N diagrams obtained for the 5 series; b-f) details of the specimens analysed respectively for series A, B, C, D and E (shown with red dots).

### 2.3 X-ray tomography detailed investigation

We investigated the samples (3 to 5 of each type) by non-destructive X-ray tomography before and after fatigue tests, after which the specimens were broken under static load (using the same setup of the fatigue testing) and then the fracture surfaces were analyzed under SEM to reveal the features that triggered the fatigue failure.

The voxel size of the microCT scan was selected as 15  $\mu\text{m}$ , allowing analysis of all pores and surface features larger than this value, and allowing a field of view covering most of the sample's critical surface. This voxel size implies that some aspects of the surface roughness is not captured, and no microstructure is visible at all as is usual for microCT. Small cracks or additional cracks which might be present (e.g. few microns only on pores) might not be visible, but this is acceptable as the largest cracks are expected to be most important.

X-ray tomography was performed using a typical laboratory microCT device at the Stellenbosch CT facility [57]. Scan parameters included 150 kV and 100  $\mu\text{A}$  for X-ray generation, with 0.5 mm copper beam filter. The sample was loaded with its long axis (Z-axis in Figure 1) vertically, rotated around this axis. A full 360 degree rotation was used for scanning in 2000 steps, at each step position the first image was discarded and the subsequent 3 images were averaged. Detector shift was enabled to minimize ring artifacts.

### 3. Analysis method

The analysis was done in two steps: i) identification and measurement of relevant surface features; ii) indexing of defect criticality. The two steps are described below.

#### 3.1 Identification and measurement of relevant surface features

Data processing and analysis was performed in Volume Graphics VGSTUDIO MAX. The use of microCT in additive manufacturing is further described in [28,58,59]. The image analysis methodology is briefly explained here. All scan data was initially de-noised using an adaptive Gaussian filter. Scans of the same sample before and after cracking were virtually overlapped using a "best-fit" registration tool, after a default surface determination of the exterior of the sample. In order to ensure the region of crack formation was well aligned for sensible analysis to be performed (e.g. for crack location after fatigue test to be correlated to surface notch features in scans prior to fatigue test), a manual refinement of the alignment was done based on local surface features and internal features (pores), such that the region of crack was well aligned. In order to find the crack origin in "before" scans, the "after" scans were viewed in slices until the location of crack origin was found in three orthogonal planes. This was not always possible within the field of view as the crack origin was sometimes at the corner of the sample, and in some cases the cracks were very narrow making accurate location identification challenging. For corner cracks, no SIF could be calculated as the reference surface for calculating effective notch depth could not be fit properly on the corner.

For cases where the crack origin was in the field of view and clearly identified, the analysis procedure was as follows. A cylinder geometry element was fitted to the exterior surface of the "before" scan data, and a duplicate volume was created of this cylinder. The original surface was compared to the best-fit cylinder volume and the result was analysed using a "nominal-actual comparison" showing maximum deviations between the rough surface and the fitted cylinder, this highlights notches (depressions) with colours indicating deviation values (also equivalent to local "thickness", or the difference between the cylinder and the actual surface). In addition, selected locations could be identified with manual annotations and these used for statistical SIF calculations (see Figure 4.a).

The procedure here implemented is very similar to the one adopted by Persenot et al. [60], who studied the initiation of fatigue failures in thin Ti6Al4V struts manufactured by EBM. In that case the authors applied an “unroll” process for the cylindrical strut-like morphology of the sample, for identifying an ideal “flat” surface for evaluating surface defect depth. The technique here adopted is similar but measures the local depth of notches directly on the geometry using a fitted geometry object, minimizing possible errors in image processing.

Since this method is only sensitive to notch depth (and not shape or width), an additional method was devised which takes half of the maximum notch depth and uses this as a criteria to assign all notches as equivalent defects, in a defect analysis function (e.g. for a surface with 100  $\mu\text{m}$  notch depth maximum, minimum 50  $\mu\text{m}$  depth used as criterion). In this way surface defects could be analysed for their horizontal extent as well as depth, and 3D images of selected “killer notches” were produced using this criteria.

This method is newly developed here and allows the identification of notches in a defect analysis function, similar to the statistical handling of porosity (each notch is treated as if it is a pore). The defect analysis function used is part of the commercial software VGSTUDIO MAX, and uses the “custom defect mask” option. The connectivity between surface notches depends on the depth of the notches and therefore a depth criterion for defining the notches as defects depends on the surface condition and is a manual step. The limit of this method is the possibility for multiple notches to be connected due to a shallow connection between them. In this work this method was used primarily for visualization and interpretation of notch geometry relative to crack location (see for example Figure 5(c)). SIF calculations were made only from notch depth, which could in principle also be measured using appropriate CT cross sectional images.

### 3.2 Indexing of defect criticality

Since the evidences in the literature showed that surface roughness and surface features could be modelled by treating the surface asperities as microcracks [37,39–41,61], the severity of the different micronotches and cavities detected by CT scan was indexed by calculating the SIF at the tip of the  $i$ -th depression below the fitted cylinder as (see Figure 4.b):

$$K_i = F \cdot S_{loc,i} \cdot \sqrt{\pi \cdot a_i} \quad (1)$$

where  $F$  is the geometric factor for semi-elliptical cracks on plates subjected to bending [62–64]  $a_i$  is the defect depth and  $S_{loc,i}$  is the prospective stress at the position (along the curved specimen’s surface) of  $i$ -th defect calculated from the Finite Element (FE) analysis of the specimen for a maximum stress  $S_{max}=100$  MPa taken as  $S_{max}=100$  MPa as a reference. This choice was made to univocally compare the defects detected on the specimens of the different series.

It was verified that Newman and Raju solution for plate bending has an error of 2% respect to SIF solution obtained with Wang & Lambert Weight Functions [65] on the real stress profile determined from FE analysis.

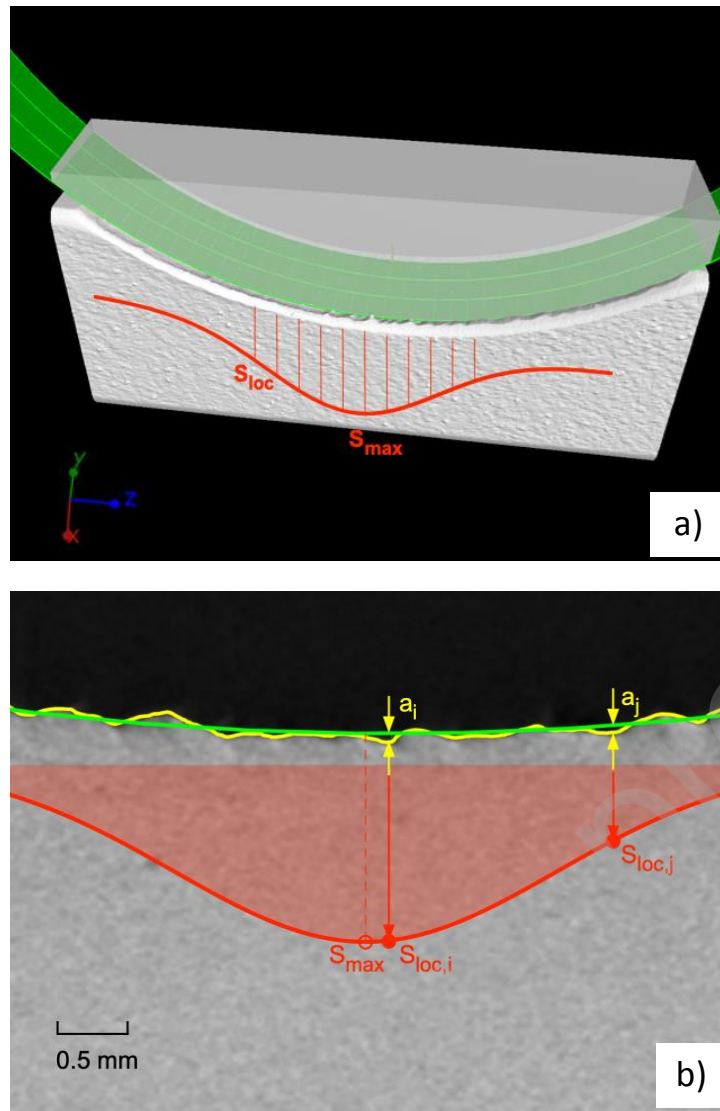


Figure 4: Scheme for detailed investigation: a) fit of a cylindrical surface to the CT surface of each specimen; b) identification of depth for surface features ( $a_i$  and  $a_j$ ) and their reference stress  $S_{loc}$  for SIF calculation.

## 4. Results

### 4.1 Detection of cracks after fatigue test

After fatigue tests, all samples showed the presence of a crack – but the crack clarity in CT images varied between sample types: A and B samples had very faint cracks indicating cracks are very narrow, while C,D and E had more clear cracks. Correlation of this with surface residual stress measurements explains the observation: C,D and E had tensile stresses on the surface, which contributes to opening the crack while the opposite is true of samples A and B which have compressive residual stress on the surface. The residual stress values are shown in Table 2.

In order to provide an overview of the 5 sample types, Figure 5 shows the microCT views in 3D and 2D cross sections for typical examples of each, showing examples of the cracks in the slice images. Table 2 shows the measured surface roughness  $R_a$  values (by traditional profilometer) for each sample type which corresponds qualitatively to the surfaces shown in 3D in Figure 5.

Overall, the roughest surfaces were those of samples A and D, with associated cracks originating at notches. In samples B, the cracks originated at sample corners and in one case on the side surface. In samples C and E, despite the smoother surfaces, notches often played a key role in the crack initiation. Each sample type and each case is discussed individually in more detail in the next sections.

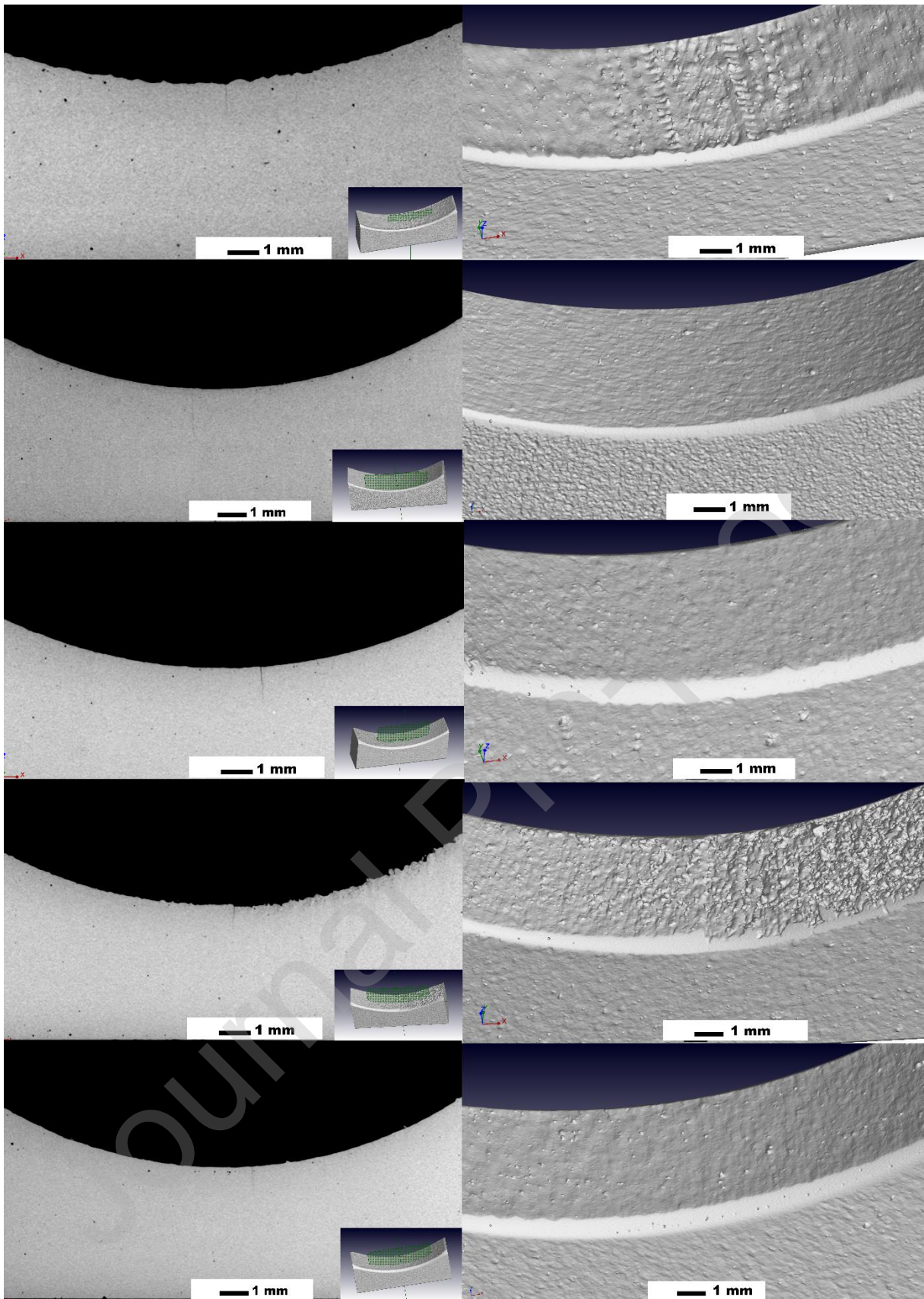


Figure 5: Examples of CT slice images and 3D images of the surfaces of samples in each series from A-E, here are shown A10, B10, C4, D2, E4.

## 4.2 Samples type A

Sample A3 is shown in Figure 6, with a colour coding according to local “thickness” of the notches or depressions as shown in Figure 6(a), with annotations showing selected notch depths. The associated SIF values for these notches are given in Figure 6(b). Figure 6(c) shows a 3D representation of the notches viewed from below, showing the “killer notch” at the location of crack initiation (annotation 1) in the red feature, which is also the widest notch in the sample. In fact, the reason for failure is not the width of the defect but the fact that it is the defect with the largest SIF on the critical surface – it is the combination of notch depth and local stress which results in higher SIF at this notch.

Sample A6 is shown in Figure 7, which clearly indicates that the crack initiates at a notch but not the largest or deepest one. This notch is elongated and its SIF does show a high value but not the highest of all notches, indicating some form of competition with another effect. In this case a subsurface pore was found at the “killer notch” and the crack runs through it as shown. The results from samples of type A (see also summary table 3) indicate the validity of the SIF calculations (considering the notches as cracks) for explaining the failure location, but the results also show competition with porosity or other notches. This is likely due to the very rough and complex surface in the critical region of the sample as seen in the 3D images of this type of surface.

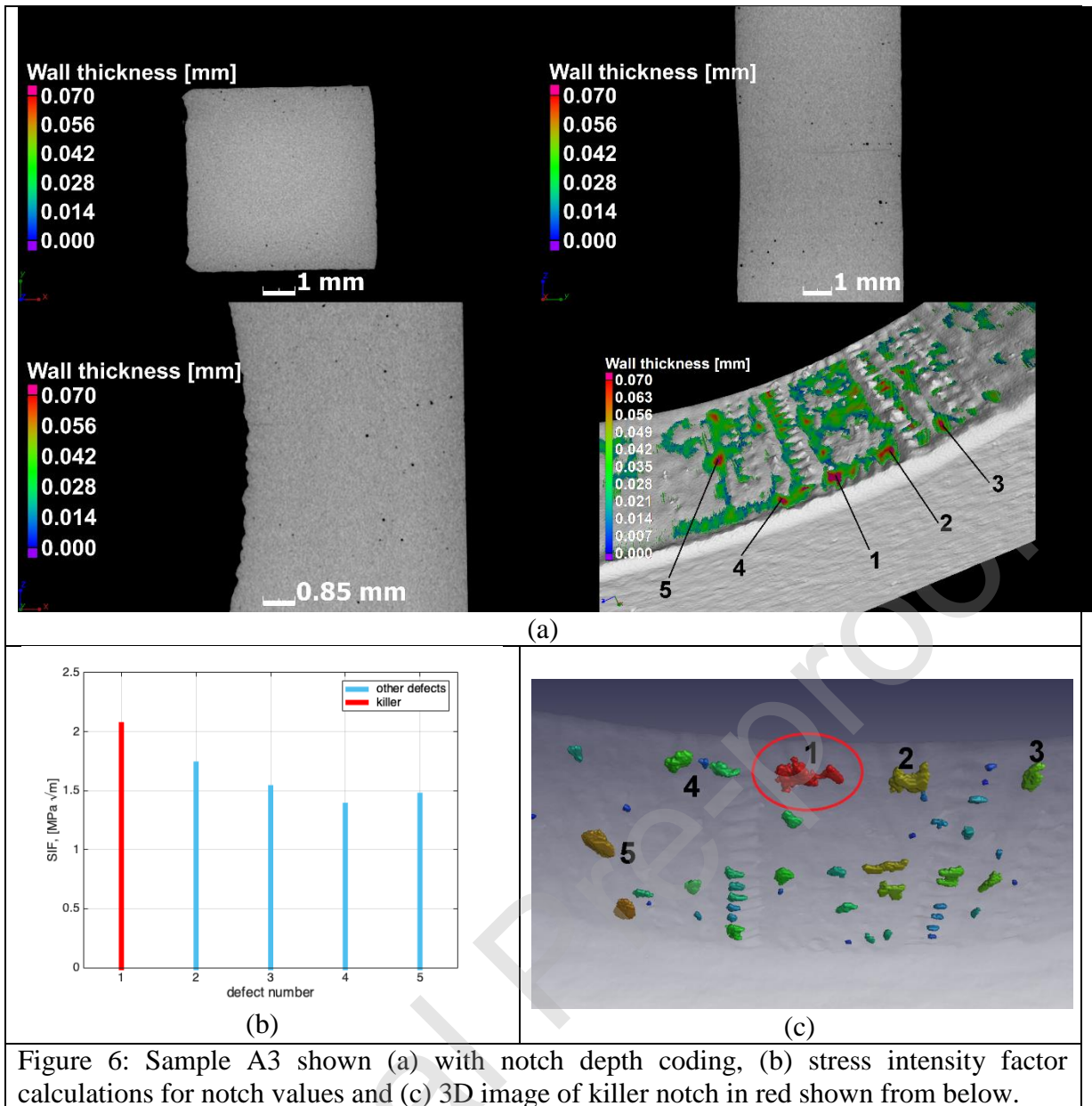


Figure 6: Sample A3 shown (a) with notch depth coding, (b) stress intensity factor calculations for notch values and (c) 3D image of killer notch in red shown from below.



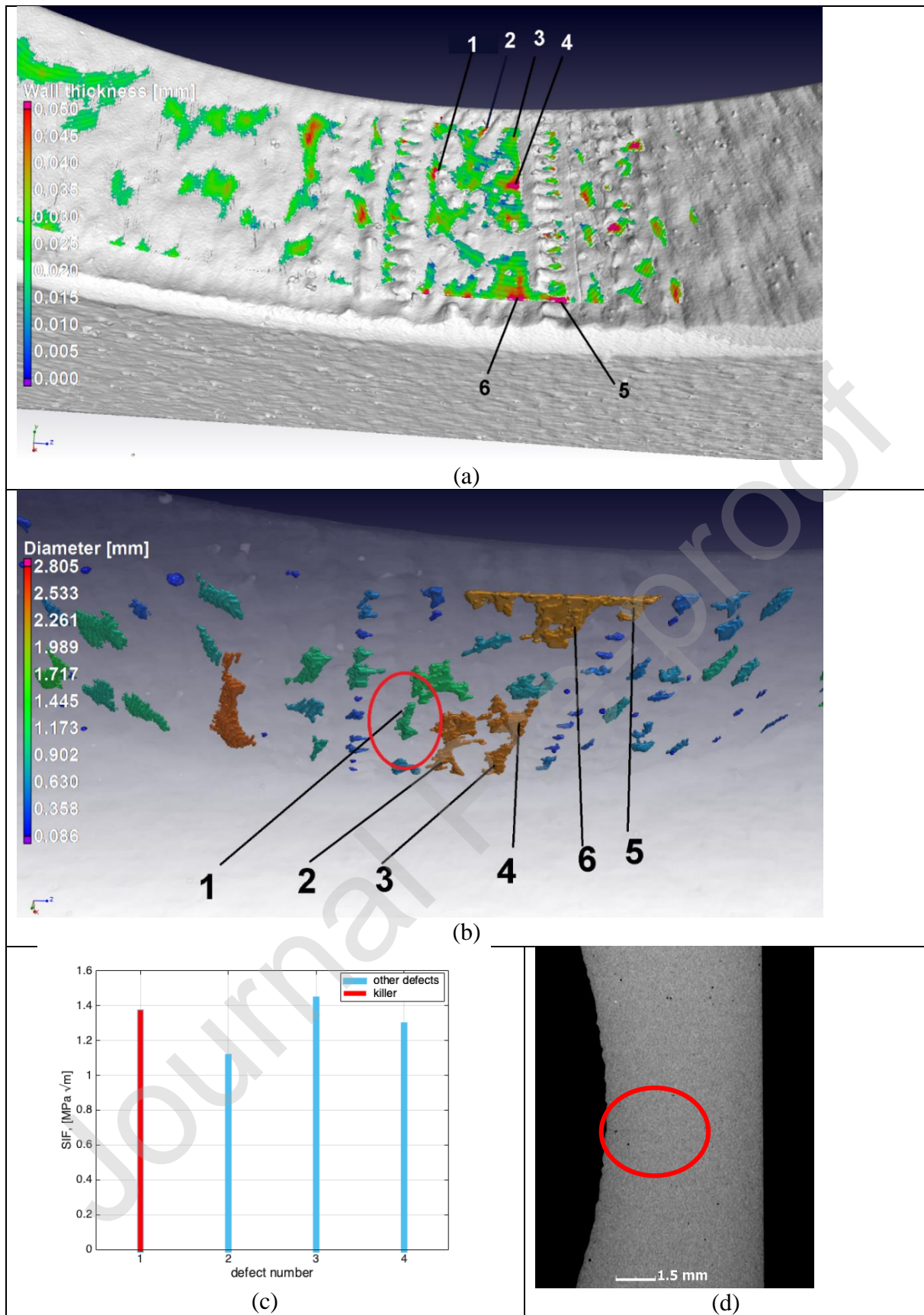


Figure 7: Sample A6 shown in (a) with color coding applied to notch regions and indicating the crack location, (b) 3D view of the killer notch in comparison to others in vicinity (c) SIF calculations indicating not the highest stress at this notch, (d) pore shown below surface which influenced this case.

### 4.3 Samples type B

In the samples of type B, the critical surface is smoother than all other types and microCT showed in two cases that the crack originates at a pore and on a notch on the side surface, this is shown in Figure 8. Two additional samples showed cracks originating from corners of the sample only, with no notch present.

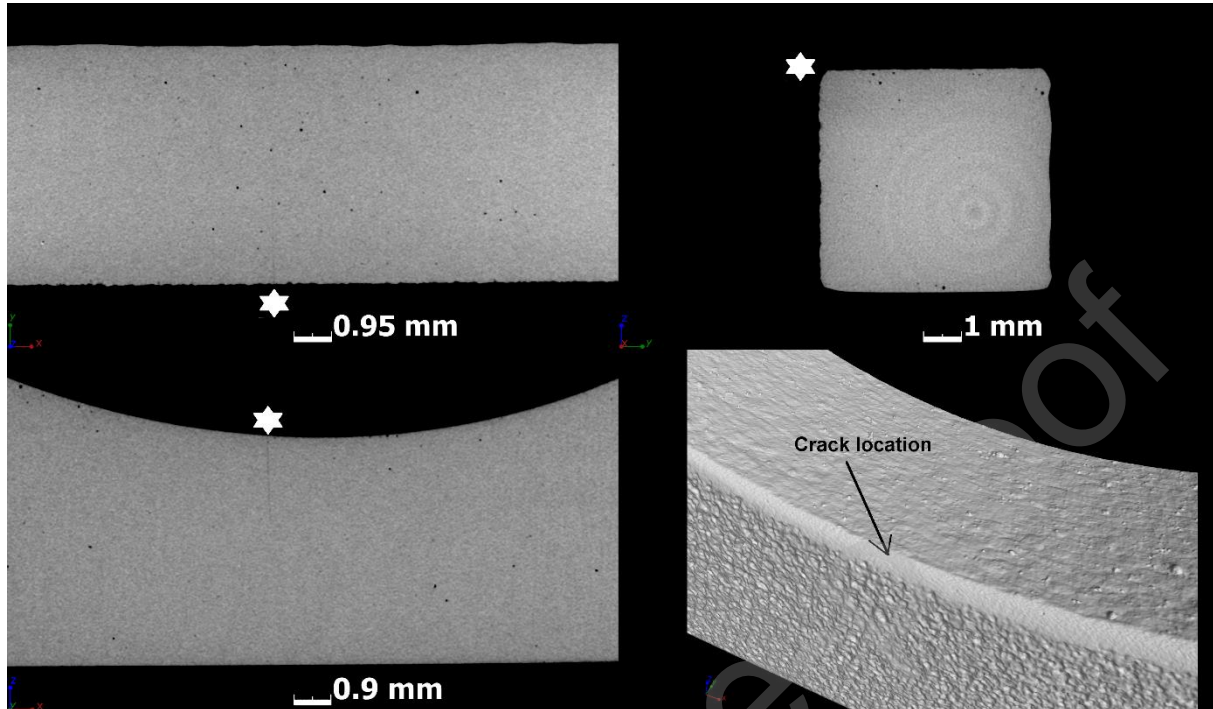


Figure 8: In samples of type B, cracks do not originate on the critical surface due to its low roughness. Here the crack originates at side surface near corner as indicated. Shown are three orthogonal views in (a)-(c) and 3D surface view in (d).

### 4.4 Samples type C

In samples of type C, cracks are wider and more easily visualized in the CT data, making direct correlation of exact crack location simpler than in samples of types A and B. Sample C1 is shown in Figure 9 and its SIF calculation explains the crack location.

Sample C2 (see Figure 10) showed two cracks whose SIF were higher than any of the other features. Figure 11 shows 3D cropped views of the main crack. Sample C4 showed a low SIF at the crack initiation location and this could be explained by the presence of a large subsurface pore in the vicinity, as shown in Figure 12.

For two other specimens, namely C3 and C5, the crack started near the corner of the specimen. No calculation was done because of the impossibility to make precise measurements near the corner. The situation is somehow similar to the B specimens, because the very low roughness for this orientation.

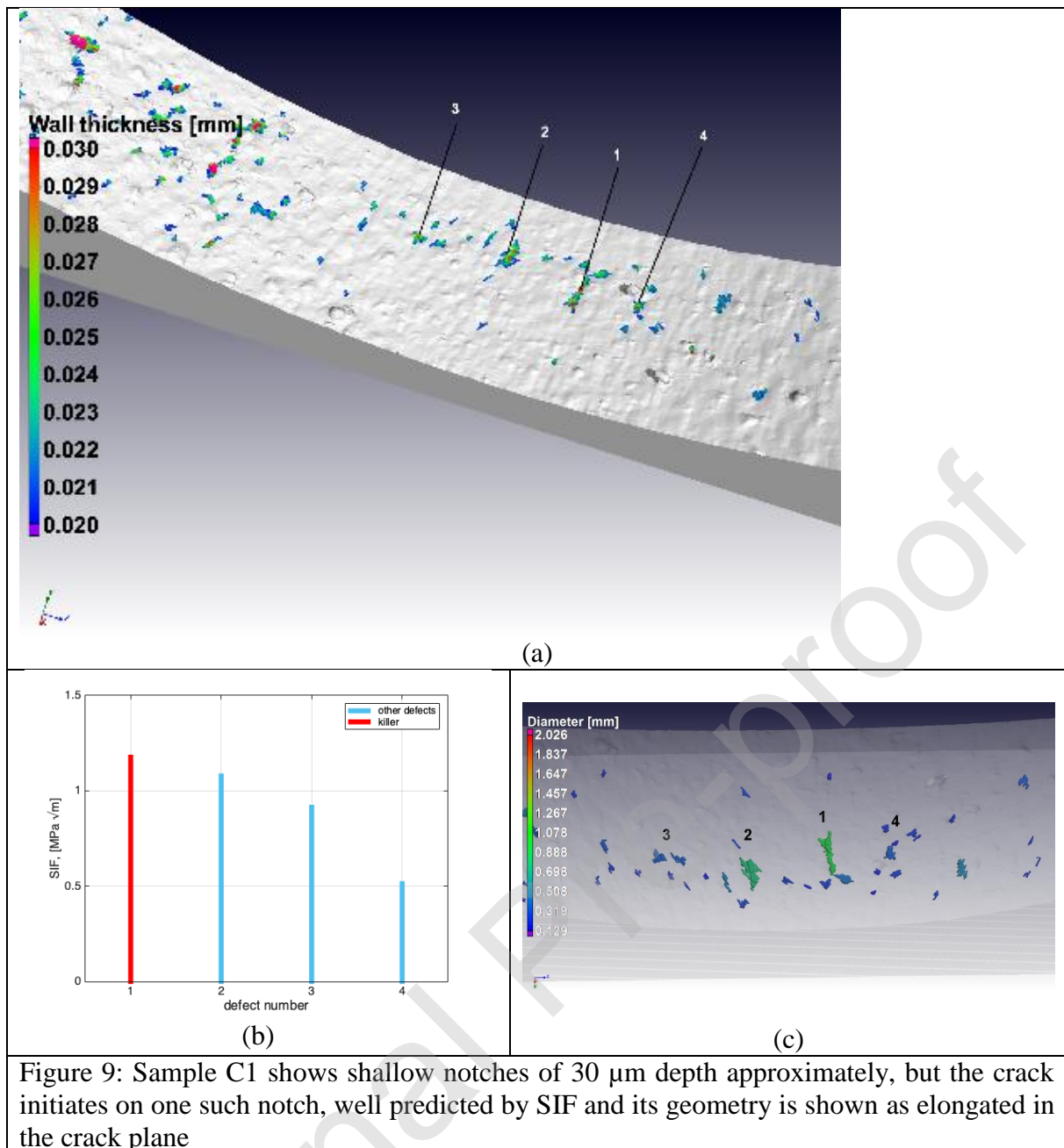


Figure 9: Sample C1 shows shallow notches of 30  $\mu\text{m}$  depth approximately, but the crack initiates on one such notch, well predicted by SIF and its geometry is shown as elongated in the crack plane

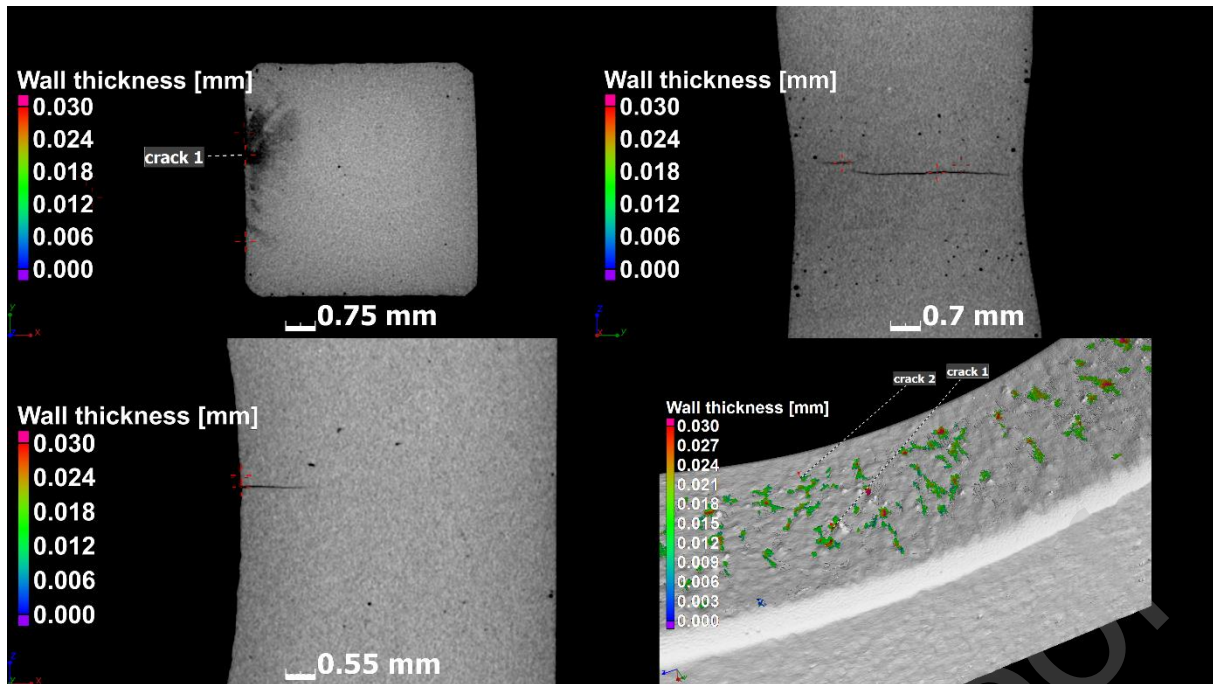


Figure 10 View of the sample C2 characterized by two cracks, whose SIF is higher than the one of the other notches. Shown are 3 orthogonal slice views in (a)-(c) and 3D surface view in (d).

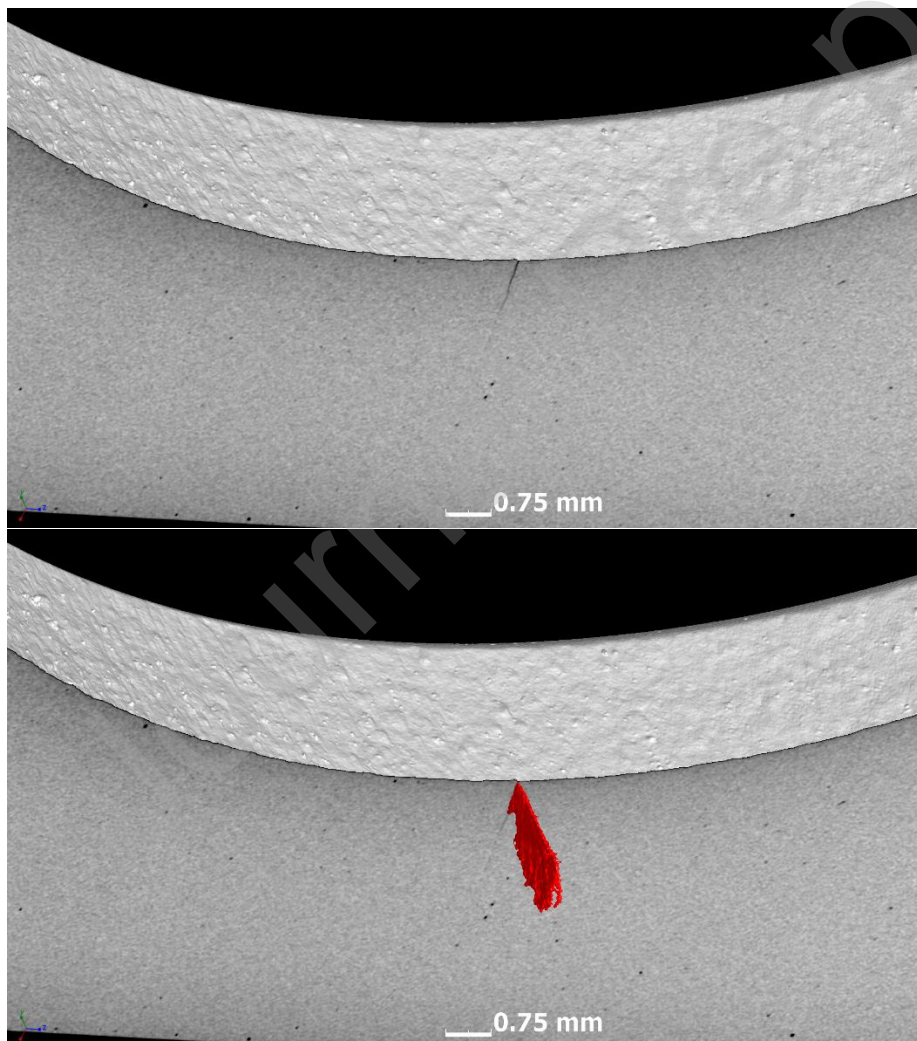


Figure 11 Enlarged 3D sectional view at the center of main crack for specimen C2, showing in (a) the crack in a virtual cross section in 3D and in (b) showing the 3D crack morphology in red. A supplementary video is provided for reader interest in 3D morphology of the crack.

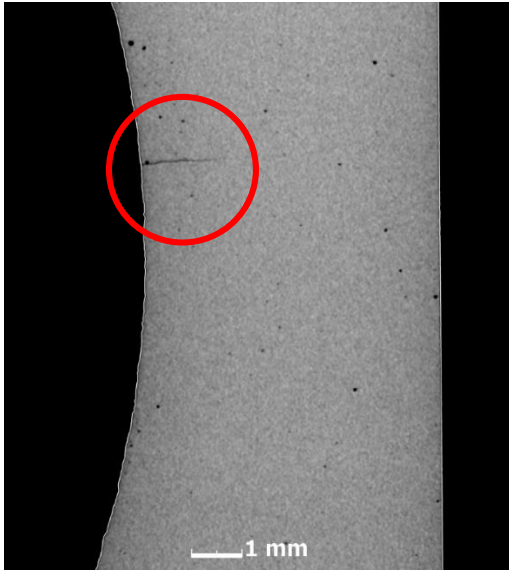


Figure 12: Sample C4 with subsurface pore explaining crack at low SIF value in this case.

Journal Pre-proof

#### 4.5 Samples type D

Samples of type D all contained a discontinuity in the center of the sample, related to some instability in powder deposition (likely caused by the presence of supports) and solidification at  $45^\circ$  in the center of the specimens, and they were also characterized with removed supports in the middle of one side of the critical surface and no supports on other side (see Figure 1.b).

The step height was measured by fitting cylinders to the two sides of the sample and measuring the difference for sample D2, giving a value of  $140\ \mu\text{m}$ . Figure 13 shows a side view of the crack location and the notch depth for sample D2, one case where the killer notch was not predicted by the simple SIF calculations according to Eq. (2) but it was essentially related to the presence of the big step, whose SIF solution (for a 2D crack) can be found in [66] and it can essentially approximated as ( $t$  being the step height):

$$K_{2d,step} = 1.12 \cdot S_{max} \cdot \sqrt{\pi \cdot t} \quad (3)$$

The samples in this batch all contained multiple cracks near or under this step location, with SIF calculations complicated by the multitude of cracks. Despite this difficulty, the cracks did initiate at notches and SIF calculations accurately predicted the location of the notches of two samples in this batch acting as “killer notches” (the SIF can be estimated with Eq. (2) when the distance from the step is larger than  $3t$ ).

As an example Sample D4 is shown in Figure 14, in this case the SIF analysis accurately predicted the 4 crack locations. As it can be seen in Figure 14(c), in reality the main crack is a coalescence of multiple initiation points (namely #1, #3 and #4).

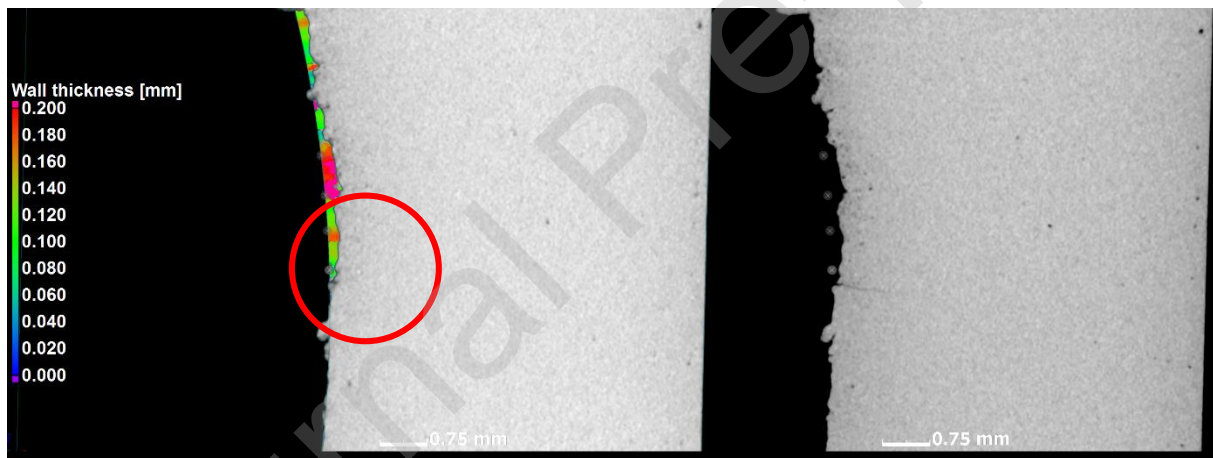


Figure 13: Sample D2 shows multiple cracks, with major one initiating at the step discontinuity.

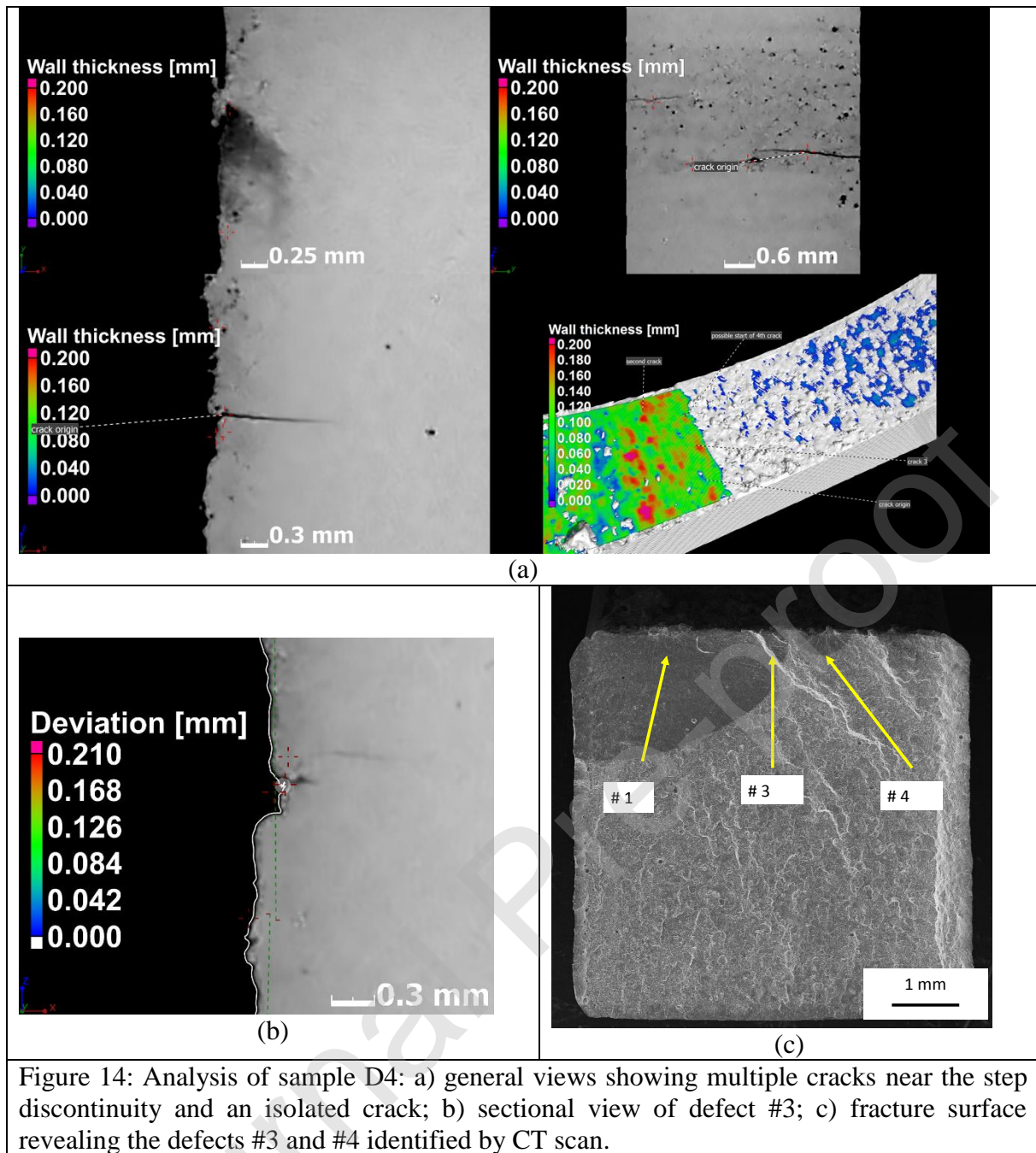


Figure 14: Analysis of sample D4: a) general views showing multiple cracks near the step discontinuity and an isolated crack; b) sectional view of defect #3; c) fracture surface revealing the defects #3 and #4 identified by CT scan.

#### 4.6 Samples type E

Samples of type E show smooth surfaces but cracks originate from shallow notches and these are explained well by the associated SIF calculations in one sample of this type. Sample E2 is shown in Figure 15, where two cracks are shown and both have equally high SIF values. The fractography reveals that the depression corresponding to the main crack has a defect below it. Other samples of this series were complicated by cracks passing through subsurface pores and not initiating on notches, indicating some competition of the crack initiation with pores in this sample type.

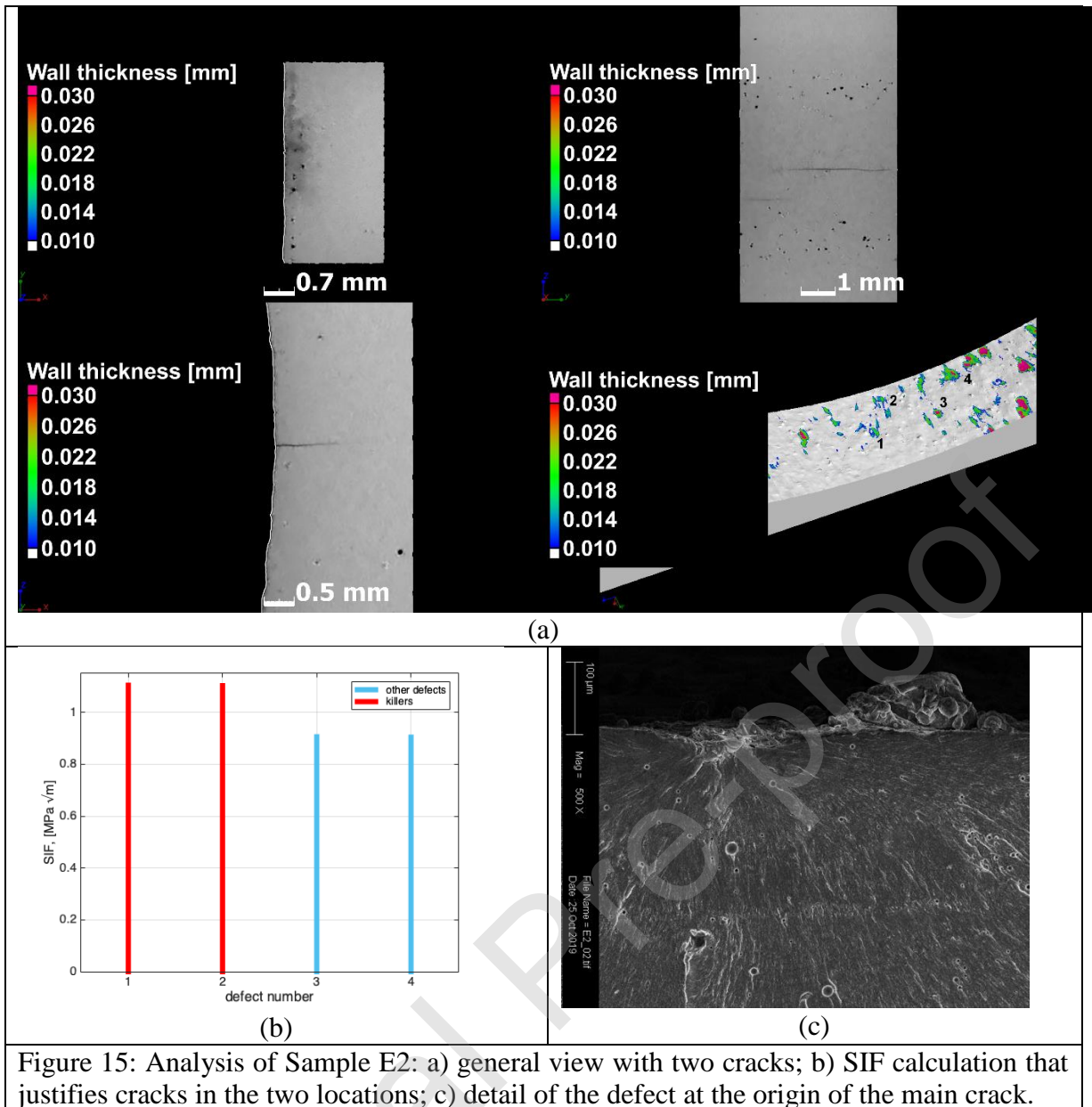


Figure 15: Analysis of Sample E2: a) general view with two cracks; b) SIF calculation that justifies cracks in the two locations; c) detail of the defect at the origin of the main crack.



## 5 Discussion

### 5.1 Summary of results

In Table 3 is summarized the results from the experimental campaign, including effective fatigue strength, and microCT-based analysis indicating the failure occurring at a notch or not, the depth of the notch associated with the primary crack, the SIF prediction success and a note about any possible pore sub-surface.

### 5.2 Remarks

It was found that, for samples of types A and D with the roughest surfaces, notches could be correlated with crack initiation in many cases, but the presence of a discontinuity in the middle of the D samples also drives multiple failures in this region and the analysis is complicated by the discontinuity. Most likely the discontinuity which is caused by the presence of supports during the build process, leads to a different thermal history in this region which leads to microstructural differences between the two sections and potentially also a complicated residual stress profile, which can contribute to crack initiation.

Samples of type B have very smooth critical surfaces and no failures were correlated with surface notches (there are effectively no notches or depressions in the surface): the failures occur in the corner of the sample or even on side surfaces which have higher roughness. Samples of type C have relatively smooth surface but shallow notches are well correlated with crack initiation, for those not initiating on corners. Samples of type E are also relatively smooth, with many failures occurring seeming to be driven by subsurface pores, except in once case where a shallow notch is identified as the crack initiation site.

It is interesting to observe that, due to bending of the specimens, the failures effectively started from the surface features and from this point of view, it looks that the assumption by Molaei et al. [40] for axial specimens that life prediction could be made considering the sum of surface plus maximum internal defect sizes is excessively conservative in the case of a stress gradient (this is due to the fact that the real probability of occurrence near the surface has to be considered [67]).

### 5.3 Consequences

The most important result of this paper is that we clearly demonstrate that failure often occurs at the features with the highest value of SIF based on surface roughness information. While the additional role of pores and other effects such as residual stress and geometry are also clear in the results, the importance of the surface features are highlighted here. This has most likely been under-estimated until now due to the lack of information on deep notches in the as-built surface by traditional surface roughness evaluation methods. The ability to predict fatigue failure based on SIF of rough surface notches backs the adoption of extreme value statistics to the sampling of surface features, as originally proposed by Murakami [68,69], in terms of sectional measurement of surface depressions/cavities.

The results clearly show the capacity offered by a full 3D analysis to capture the surface features and that the failures could be explained by SIF only, considering also the width of the defect (a feature only offered by 3D measurements). This means that sectional measurements for AM surfaces [19,61] are perhaps too simple and that an areal “extreme value” sampling (that means capturing the maximum defect on portions of the surface) of surface features is the right direction (as proposed in [32] for capturing the largest stress concentrations).

It must be emphasised that the significance of these results are in realization of the importance of surface roughness on the fatigue properties, and that the actual surface details revealed by

CT scans allows a predictive failure analysis, which has not been reported before. This assists in the understanding of the effect of rough as-built surfaces on the fatigue properties, which is highly important for complex parts where no post-processing can be applied to hidden surfaces.

## 6 Conclusions

In this work a new methodology of quantifying surface notches was demonstrated using microCT data of as-built surfaces of additively manufactured AlSi10Mg specimens. An experimental campaign was reported where the deepest notches were measured and stress intensity factor calculations used to correlate notches with fatigue crack initiation for five different types of surface roughness, due to different build orientations. Despite expected competing effects of subsurface pores, microstructure and residual stresses, the method accurately predicts 7 failure locations, with 4 cases of failure at locations other than the highest stress intensity factor.

It was found that notches deeper than 50  $\mu\text{m}$  have a high likelihood of acting as crack initiation location irrespective of the surface quality, and these can be identified by comparing the surface with a mean surface (or geometric fitted object) in microCT data. This provides not only a visual identification of surface notch locations but also allows quantitative evaluation of the local depth of the notches, for stress intensity factor calculations as demonstrated.

The importance of this work is that it demonstrates the ability to quantify the rough as-built surface information, and effective notch depths in particular, and use these for predictive fatigue analysis. This work lays the foundation for the development of prediction models of fatigue failure of additively manufactured parts based on as-built surfaces, and for improvement of the properties by surface modification. Future work is envisaged whereby samples with and without subsurface pores are manufactured, and with samples which have been subjected to stress relief. This will assist in understanding the role of each manufacturing defect type and the importance of each, helping to design fatigue-resistant parts in complex as-built geometries in future.

## Acknowledgements

The Collaborative Program for Additive Manufacturing (CPAM), funded by the South African Department of Science and technology, is acknowledged for financial support of AdP. Support by the Italian Ministry for Education, University and Research through the project Department of Excellence LIS4.0 (Lightweight and Smart Structures for Industry 4.0) is also acknowledged. The authors acknowledge support by Mr. Mostafa Gargourimothlagh (PoliMi) for mechanical tests help with analysis of fatigue data, Ms. Muofhe Tshibalanganda and Ms. Carlyn Wells for support with microCT scans.

The authors acknowledge support by BEAMIT (Fornovo, Italy) for specimen supply and careful preparation. We also thank the four anonymous reviewers and editor for helpful comments.

## Data availability

The microCT data of each sample before and after fatigue test is made available on request, in the form of aligned image stacks at 15  $\mu\text{m}$  voxel size. This data has no image processing applied which makes it suitable for investigations other than that reported in this paper.

## Conflict of Interest Statement

One of the authors of this article is part of the editorial board of the journal. To avoid potential conflicts of interest, the responsibility for the editorial and peer-review process of this article lies with the other editors of the journal. Furthermore, the authors of this article were removed from the peer review process and have no access to confidential information related to the editorial process of this article.

## References

- [1] T. Debroy, H.L. Wei, J.S. Zuback, T. Mukherjee, J.W. Elmer, J.O. Milewski, A.M. Beese, A. Wilson-Heid, A. De, W. Zhang, Additive manufacturing of metallic components – Process, structure and properties, *Prog. Mater. Sci.* 92 (2018) 112–224. doi:10.1016/j.pmatsci.2017.10.001.
- [2] T. DebRoy, T. Mukherjee, J.O. Milewski, J.W. Elmer, B. Ribic, J.J. Blecher, W. Zhang, Scientific, technological and economic issues in metal printing and their solutions, *Nat. Mater.* (2019) 1. doi:10.1038/s41563-019-0408-2.
- [3] I. Yadroitsev, P. Krakhmalev, I. Yadroitsava, A. Du Plessis, Qualification of Ti6Al4V ELI Alloy Produced by Laser Powder Bed Fusion for Biomedical Applications, *JOM.* 70 (2018) 372–377. doi:10.1007/s11837-017-2655-5.
- [4] D. Bourell, J.P. Kruth, M. Leu, G. Levy, D. Rosen, A.M. Beese, A. Clare, Materials for additive manufacturing, *CIRP Ann.* 66 (2017) 659–681. doi:10.1016/J.CIRP.2017.05.009.
- [5] J.J. Lewandowski, M. Seifi, Metal Additive Manufacturing: A Review of Mechanical Properties, *Annu. Rev. Mater. Res.* 46 (2016) 151–186. doi:10.1146/annurev-matsci-070115-032024.
- [6] M. Seifi, A. Salem, J. Beuth, O. Harrysson, J.J. Lewandowski, Overview of Materials Qualification Needs for Metal Additive Manufacturing, *JOM.* 68 (2016) 747–764. doi:10.1007/s11837-015-1810-0.
- [7] Y. Murakami, *Metal fatigue: effects of small defects and nonmetallic inclusions*, Elsevier, 2002.
- [8] U. Zerbst, M. Madia, C. Klinger, D. Bettge, Y. Murakami, Defects as a root cause of fatigue failure of metallic components. I: Basic aspects, *Eng. Fail. Anal.* 97 (2019) 777–792. doi:10.1016/j.engfailanal.2019.01.055.
- [9] U. Zerbst, M. Madia, C. Klinger, D. Bettge, Y. Murakami, Defects as a root cause of fatigue failure of metallic components. II: Non-metallic inclusions, *Eng. Fail. Anal.* (2019) 1–12. doi:10.1016/j.engfailanal.2019.01.054.
- [10] Y. Murakami, C. Klinger, M. Madia, U. Zerbst, D. Bettge, Defects as a root cause of fatigue failure of metallic components. III: Cavities, dents, corrosion pits, scratches, *Eng. Fail. Anal.* 97 (2019) 759–776. doi:10.1016/j.engfailanal.2019.01.034.
- [11] A. du Plessis, I. Yadroitsava, I. Yadroitsev, Effects of defects on mechanical properties in metal additive manufacturing: A review focusing on X-ray tomography insights, *Mater. Des.* 187 (2020). doi:10.1016/j.matdes.2019.108385.
- [12] M. Hamidi Nasab, S. Romano, D. Gastaldi, S. Beretta, M. Vedani, Combined effect of surface anomalies and volumetric defects on fatigue assessment of AlSi7Mg fabricated via laser powder bed fusion, *Addit. Manuf.* (2019) 100918. doi:10.1016/j.addma.2019.100918.
- [13] A. Yadollahi, N. Shamsaei, Additive manufacturing of fatigue resistant materials: Challenges and opportunities, *Int. J. Fatigue.* 98 (2017) 14–31. doi:10.1016/j.ijfatigue.2017.01.001.
- [14] S. Romano, A. Brandão, J. Gumpinger, M. Gschweidl, S. Beretta, Qualification of AM parts: Extreme value statistics applied to tomographic measurements, *Mater. Des.* 131 (2017) 32–48. doi:10.1016/J.MATDES.2017.05.091.
- [15] S. Romano, A. Brückner-Foit, A. Brandão, J. Gumpinger, T. Ghidini, S. Beretta, Fatigue properties of AlSi10Mg obtained by additive manufacturing: Defect-based modelling and prediction of fatigue strength, *Eng. Fract. Mech.* 187 (2018) 165–189. doi:10.1016/j.engfracmech.2017.11.002.
- [16] M. Hamidi Nasab, A. Giussani, D. Gastaldi, V. Tirelli, M. Vedani, Effect of Surface and Subsurface Defects on Fatigue Behavior of AlSi10Mg Alloy Processed by Laser

- Powder Bed Fusion (L-PBF), *Metals* (Basel). 9 (2019) 1063. doi:10.3390/met9101063.
- [17] Y. Murakami, H. Masuo, Y. Tanaka, M. Nakatani, Defect Analysis for Additively Manufactured Materials in Fatigue from the Viewpoint of Quality Control and Statistics of Extremes, *Procedia Struct. Integr.* 19 (2019) 113–122. doi:10.1016/j.prostr.2019.12.014.
- [18] Y.N. Hu, S.C. Wu, Z.K. Wu, X.L. Zhong, S. Ahmed, S. Karabal, X.H. Xiao, H.O. Zhang, P.J. Withers, A new approach to correlate the defect population with the fatigue life of selective laser melted Ti-6Al-4V alloy, *Int. J. Fatigue.* 136 (2020) 105584. doi:10.1016/j.ijfatigue.2020.105584.
- [19] H. Masuo, Y. Tanaka, S. Morokoshi, H. Yagura, T. Uchida, Y. Yamamoto, Y. Murakami, Influence of defects, surface roughness and HIP on the fatigue strength of Ti-6Al-4V manufactured by additive manufacturing, *Int. J. Fatigue.* 117 (2018) 163–179. doi:10.1016/j.ijfatigue.2018.07.020.
- [20] A. du Plessis, D. Glaser, H. Moller, N. Mathe, L. Tshabalala, B. Mfusi, R. Mostert, Pore Closure Effect of Laser Shock Peening of Additively Manufactured AlSi10Mg, *3D Print. Addit. Manuf.* 6 (2019). doi:10.1089/3dp.2019.0064.
- [21] D. Glaser, C. Polese, R.D. Bedekar, J. Plaisier, S. Pityana, B. Masina, T. Mathebula, E. Troiani, Laser Shock Peening on a 6056-T4 Aluminium Alloy for Airframe Applications, *Adv. Mater. Res.* 891–892 (2014) 974–979. doi:10.4028/www.scientific.net/amr.891-892.974.
- [22] A. du Plessis, C. Broeckhoven, I. Yadroitsava, I. Yadroitsev, C.H. Hands, R. Kunju, D. Bhate, Beautiful and Functional: A Review of Biomimetic Design in Additive Manufacturing, *Addit. Manuf.* 27 (2019) 408–427. doi:10.1016/j.addma.2019.03.033.
- [23] G. Strano, L. Hao, R.M. Everson, K.E. Evans, Surface roughness analysis, modelling and prediction in selective laser melting, *J. Mater. Process. Technol.* 213 (2013) 589–597. doi:10.1016/j.jmatprotec.2012.11.011.
- [24] G. Nicoletto, R. Konečná, M. Frkáň, E. Riva, Surface roughness and directional fatigue behavior of as-built EBM and DMLS Ti6Al4V, *Int. J. Fatigue.* 116 (2018) 140–148. doi:10.1016/j.ijfatigue.2018.06.011.
- [25] J. Pegues, M. Roach, R. Scott Williamson, N. Shamsaei, Surface roughness effects on the fatigue strength of additively manufactured Ti-6Al-4V, *Int. J. Fatigue.* 116 (2018) 543–552. doi:10.1016/j.ijfatigue.2018.07.013.
- [26] K. Solberg, F. Berto, A diagram for capturing and predicting failure locations in notch geometries produced by additive manufacturing, *Int. J. Fatigue.* 134 (2020) 105428. doi:10.1016/j.ijfatigue.2019.105428.
- [27] M. Benedetti, C. Santus, Notch fatigue and crack growth resistance of Ti-6Al-4V ELI additively manufactured via selective laser melting: A critical distance approach to defect sensitivity, *Int. J. Fatigue.* 121 (2019) 281–292. doi:10.1016/j.ijfatigue.2018.12.020.
- [28] A. du Plessis, I. Yadroitsev, I. Yadroitsava, S.G. Le Roux, X-Ray Microcomputed Tomography in Additive Manufacturing: A Review of the Current Technology and Applications, *3D Print. Addit. Manuf.* 5 (2018) 3dp.2018.0060. doi:10.1089/3dp.2018.0060.
- [29] J.-Y. Buffiere, E. Maire, J. Adrien, J.-P. Masse, E. Boller, In Situ Experiments with X ray Tomography: an Attractive Tool for Experimental Mechanics, *Exp. Mech.* 50 (2010) 289–305. doi:10.1007/s11340-010-9333-7.
- [30] J.Y. Buffiere, Fatigue Crack Initiation and Propagation from Defects in Metals: Is 3D Characterization Important?, *Procedia Struct. Integr.* 7 (2017) 27–32. doi:10.1016/j.prostr.2017.11.056.
- [31] T. Persenot, A. Burr, G. Martin, J.Y. Buffiere, R. Dendievel, E. Maire, Effect of build orientation on the fatigue properties of as-built Electron Beam Melted Ti-6Al-4V alloy, *Int. J. Fatigue.* 118 (2019) 65–76. doi:10.1016/j.ijfatigue.2018.08.006.

- [32] W. Schneller, M. Leitner, S. Pomberger, S. Springer, F. Beter, F. Grün, Effect of Post Treatment on the Microstructure, Surface Roughness and Residual Stress Regarding the Fatigue Strength of Selectively Laser Melted AlSi10Mg Structures, *J. Manuf. Mater. Process.* 3 (2019) 89. doi:10.3390/jmmp3040089.
- [33] J.W. Pegues, N. Shamsaei, M.D. Roach, R.S. Williamson, Fatigue life estimation of additive manufactured parts in the as-built surface condition, *Mater. Des. Process. Commun.* 1 (2019) e36. doi:10.1002/mdp2.36.
- [34] B. Vayssette, N. Saintier, C. Brugger, M. El May, E. Pessard, Numerical modelling of surface roughness effect on the fatigue behavior of Ti-6Al-4V obtained by additive manufacturing, *Int. J. Fatigue.* 123 (2019) 180–195. doi:10.1016/j.ijfatigue.2019.02.014.
- [35] G.W. Zeng, M.C. Monu, C. Lupton, B. Lin, J. Tong, Towards a fundamental understanding of the effects of surface conditions on fatigue resistance for safety-critical AM applications, *Int. J. Fatigue.* 136 (2020) 105585. doi:10.1016/j.ijfatigue.2020.105585.
- [36] E. Wycisk, A. Solbach, S. Siddique, D. Herzog, F. Walther, C. Emmelmann, Effects of defects in laser additive manufactured Ti-6Al-4V on fatigue properties, in: *Phys. Procedia*, Elsevier B.V., 2014: pp. 371–378. doi:10.1016/j.phpro.2014.08.120.
- [37] D. Greitemeier, C. Dalle Donne, F. Syassen, J. Eufinger, T. Melz, Effect of surface roughness on fatigue performance of additive manufactured Ti-6Al-4V, *Mater. Sci. Technol.* 32 (2016) 629–634. doi:10.1179/1743284715Y.0000000053.
- [38] D. Greitemeier, F. Palm, F. Syassen, T. Melz, Fatigue performance of additive manufactured TiAl6V4 using electron and laser beam melting, *Int. J. Fatigue.* 94 (2017) 211–217. doi:10.1016/j.ijfatigue.2016.05.001.
- [39] A. Yadollahi, M.J. Mahtabi, A. Khalili, H.R. Doude, J.C. Newman, Fatigue life prediction of additively manufactured material: Effects of surface roughness, defect size, and shape, *Fatigue Fract. Eng. Mater. Struct.* 41 (2018) 1602–1614. doi:10.1111/ffe.12799.
- [40] R. Molaei, A. Fatemi, N. Sanaei, J. Pegues, N. Shamsaei, S. Shao, P. Li, D.H. Warner, N. Phan, Fatigue of additive manufactured Ti-6Al-4V, Part II: The relationship between microstructure, material cyclic properties, and component performance, *Int. J. Fatigue.* 132 (2020) 105363. doi:10.1016/j.ijfatigue.2019.105363.
- [41] J. Zhang, A. Fatemi, Surface roughness effect on multiaxial fatigue behavior of additive manufactured metals and its modeling, *Theor. Appl. Fract. Mech.* 103 (2019) 102260. doi:10.1016/j.tafmec.2019.102260.
- [42] S. Romano, P.D. Nezhadfar, N. Shamsaei, M. Seifi, S. Beretta, High cycle fatigue behavior and life prediction for additively manufactured 17-4 PH stainless steel: Effect of sub-surface porosity and surface roughness, *Theor. Appl. Fract. Mech.* 106 (2020) 102477. doi:10.1016/j.tafmec.2020.102477.
- [43] J. Gockel, L. Sheridan, B. Koerper, B. Whip, The influence of additive manufacturing processing parameters on surface roughness and fatigue life, *Int. J. Fatigue.* 124 (2019) 380–388. doi:10.1016/j.ijfatigue.2019.03.025.
- [44] Y. Murakami, Inclusion Rating by Statistics of Extreme Values and Its Application to Fatigue Strength Prediction and Quality Control of Materials, n.d. [https://nvlpubs.nist.gov/nistpubs/jres/099/jresv99n4p345\\_A1b.pdf](https://nvlpubs.nist.gov/nistpubs/jres/099/jresv99n4p345_A1b.pdf) (accessed March 16, 2020).
- [45] S. Beretta, Y. Murakami, Statistical analysis of defects for fatigue strength prediction and quality control of materials, *Fatigue Fract. Eng. Mater. Struct.* 21 (1998) 1049–1065. doi:10.1046/j.1460-2695.1998.00104.x.
- [46] ASTM E2283 - 08(2019) Standard Practice for Extreme Value Analysis of Nonmetallic Inclusions in Steel and Other Microstructural Features, (n.d.). <https://www.astm.org/Standards/E2283.htm> (accessed March 16, 2020).

- [47] S. Beretta, Fatigue strength assessment and surface rating for "as built" AlSi10Mg manufactured by SLM with different build orientations, *Int. J. Fatigue*. (n.d.).
- [48] ASTM D7127 - 17 Standard Test Method for Measurement of Surface Roughness of Abrasive Blast Cleaned Metal Surfaces Using a Portable Stylus Instrument, (n.d.). <https://www.astm.org/Standards/D7127.htm> (accessed March 18, 2020).
- [49] J.L. Bartlett, X. Li, An overview of residual stresses in metal powder bed fusion, *Addit. Manuf.* 27 (2019) 131–149. doi:10.1016/j.addma.2019.02.020.
- [50] C. Li, Z.Y. Liu, X.Y. Fang, Y.B. Guo, Residual Stress in Metal Additive Manufacturing, *Procedia CIRP*. 71 (2018) 348–353. doi:10.1016/j.procir.2018.05.039.
- [51] M. Gargourimotlagh, FATIGUE BEHAVIOR OF ADDITIVELY MANUFACTURED ALSI10MG ALLOYS: AN ASSESSMENT OF THE SURFACE ROUGHNESS EFFECT, Politecnico di Milano, 2019.
- [52] ASTM International, ASTM E739-10(2015) Standard Practice for Statistical Analysis of Linear or Linearized Stress-Life (S-N) and Strain-Life ( $\epsilon$ -) Fatigue Data, *Annu. B. ASTM Stand.* i (2015) 1–7. doi:10.1520/E0739-10R15.
- [53] W.J. Dixon, The Up-and-Down Method for Small Samples, *J. Am. Stat. Assoc.* 60 (1965) 967–978. doi:10.1080/01621459.1965.10480843.
- [54] E. Brandl, U. Heckenberger, V. Holzinger, D. Buchbinder, Additive manufactured AlSi10Mg samples using Selective Laser Melting (SLM): Microstructure, high cycle fatigue, and fracture behavior, *Mater. Des.* 34 (2012) 159–169. doi:10.1016/j.matdes.2011.07.067.
- [55] T.M. Mower, M.J. Long, Mechanical behavior of additive manufactured, powder-bed laser-fused materials, *Mater. Sci. Eng. A*. 651 (2016) 198–213. doi:10.1016/j.msea.2015.10.068.
- [56] G. Nicoletto, INFLUENCE OF ROUGH AS-BUILT SURFACES ON SMOOTH AND NOTCHED FATIGUE BEHAVIOR OF L-PBF AlSi10Mg, *Addit. Manuf.* 34 (2020) 101251. doi:10.1016/j.addma.2020.101251.
- [57] A. du Plessis, S.G. le Roux, A. Guelpa, The CT Scanner Facility at Stellenbosch University: An open access X-ray computed tomography laboratory, *Nucl. Instruments Methods Phys. Res. Sect. B Beam Interact. with Mater. Atoms.* 384 (2016) 42–49. doi:10.1016/j.nimb.2016.08.005.
- [58] A. du Plessis, S.G. le Roux, Standardized X-ray tomography testing of additively manufactured parts: A round robin test, *Addit. Manuf.* 24 (2018) 125–136. doi:10.1016/j.addma.2018.09.014.
- [59] A. du Plessis, S.G. le Roux, J. Waller, P. Sperling, N. Achilles, A. Beerlink, J.F. Métayer, M. Sinico, G. Probst, W. Dewulf, F. Bittner, H.J. Endres, M. Willner, Á. Drégelyi-Kiss, T. Zikmund, J. Laznovsky, J. Kaiser, P. Pinter, S. Dietrich, E. Lopez, O. Fitzek, P. Konrad, Laboratory X-ray tomography for metal additive manufacturing: Round robin test, *Addit. Manuf.* 30 (2019) 100837. doi:10.1016/j.addma.2019.100837.
- [60] T. Persenot, A. Burr, R. Dendievel, J.Y. Buffière, E. Maire, J. Lachambre, G. Martin, Fatigue performances of chemically etched thin struts built by selective electron beam melting: Experiments and predictions, *Materialia*. 9 (2020) 100589. doi:10.1016/j.mtla.2020.100589.
- [61] H. Masuo, Y. Tanaka, S. Morokoshi, H. Yagura, T. Uchida, Y. Yamamoto, Y. Murakami, Effects of Defects, Surface Roughness and HIP on Fatigue Strength of Ti-6Al-4V manufactured by Additive Manufacturing, *Procedia Struct. Integr.* 7 (2017) 19–26. doi:10.1016/j.prostr.2017.11.055.
- [62] I.S. Raju, J.C. Newman, Stress-intensity factors for a wide range of semi-elliptical surface cracks in finite-thickness plates, *Eng. Fract. Mech.* 11 (1979) 817–829. doi:10.1016/0013-7944(79)90139-5.
- [63] J.C. Newman, I.S. Raju, An empirical stress-intensity factor equation for the surface crack, *Eng. Fract. Mech.* 15 (1981) 185–192. doi:10.1016/0013-7944(81)90116-8.

- [64] J. Newman, ... I.R.-: F.S.I.T. and, undefined 1983, Stress-intensity factor equations for cracks in three-dimensional finite bodies, Astm.Org. (n.d.). [http://www.astm.org/DIGITAL\\_LIBRARY/STP/PAGES/STP37074S.htm](http://www.astm.org/DIGITAL_LIBRARY/STP/PAGES/STP37074S.htm) (accessed May 3, 2020). (this reference does not look correct)
- [65] X. Wang, S.B. Lambert, Stress intensity factors for low aspect ratio semi-elliptical surface cracks in finite-thickness plates subjected to nonuniform stresses, *Eng. Fract. Mech.* 51 (1995) 517–532. doi:10.1016/0013-7944(94)00311-5.
- [66] Y. Murakami, *Stress intensity factors handbook*, Pergamon, 1987.
- [67] S. Romano, S. Miccoli, S. Beretta, A new FE post-processor for probabilistic fatigue assessment in the presence of defects and its application to AM parts, *Int. J. Fatigue.* 125 (2019) 324–341. doi:10.1016/j.ijfatigue.2019.04.008.
- [68] Y. Murakami, K. Takahashi, T. Yamashita, Quantitative evaluation of the effect of surface roughness, *Trans. Japan Soc. Mech. Eng. Series A* 6 (1997) 12–19.
- [69] K. Takahashi, Y. Murakami, Quantitative evaluation of effect of surface roughness on fatigue strength, *Eng. against Fatigue.* (1999) 693–703.

Tab. 1: Tensile properties along the three main orientations [47]

orientation	Sy [MPa]	UTS [MPa]
0° (series A)	229	379.5
45° (series D and E)	206	383
90° (series C)	208	396

Table 2: Measured surface roughness ( $R_a$  and  $R_z$ ) values for each sample type

Sample type	$R_a$ $\mu \pm 2\sigma$ ( $\mu\text{m}$ )	$R_z$ $\mu \pm 2\sigma$ ( $\mu\text{m}$ )
A	$8.04 \pm 4.4$	$27.028 \pm 16.3$
B	$2.72 \pm 1.14$	$12.748 \pm 5.42$
C	$2.97 \pm 0.92$	$12.429 \pm 4.04$
D	$7.05 \pm 4.73$	$29.186 \pm 19.14$
E	$3.06 \pm 1.84$	$14.232 \pm 8.86$

Table 2: Residual stress of each sample type (measured on two specimens per series)

Sample type	Residual stress (MPa)	Deviation (MPa)	FWHM (deg)
A	-6.9	$\pm 10.3$	1.42
B	-14	$\pm 9.4$	1.45
C	167.7	$\pm 20.1$	1.40
D	150.65	$\pm 40.1$	1.25
E	98.6	$\pm 14.6$	1.35

Table 3: Fatigue limits  $\Delta S_{lim}$  for the different specimen series

Series	Fatigue limit $\Delta S_{lim}$ , MPa
A	122
B	144
C	97
D	50
E	134



Table 3: Summary of microCT data of “killer notches”

Sample	Effective applied stress $\Delta S$ (MPa)	$\Delta S/\Delta S_{lim}$	Fail at notch?	Notch depth ( $\mu m$ )	SIF prediction	Possibly affected by pore?
A3	138	1.13	Yes	116	Yes	-
A6	147	1.20	Yes	51	No	Yes
A10	123	1.01	Yes	88	Yes	-
B9	169	1.17	No, corner	-		
B10	158	1.10	No, side surface	-		
B11	196	1.36	No, corner	-		
B12	149	1.03	No, corner	-		
C1	148	1.52	Yes	32	Yes	-
C2	150	1.54	Yes	26	Yes	-
C3	120	1.23	Yes but near corner	-		
C4	111	1.14	Yes	24	No	Yes
C5	104	1.07	Yes but near corner	-		
D1	70	1.40	Yes, deep notch on corner, no analysis done	-		
D2	119	2.38	Yes, at step	159	No	-
D3	90	1.80	Yes, at step	195	Yes	-
D4	65	1.30	Yes, at step	192	Yes	-
D5	49	0.98	Yes, at step & notch	230	No	Yes
E2	159	1.18	Yes	33	Yes	-
E3	134.5	1.00	No, possibly on pore	-	-	Yes
E4	164	1.22	No, possibly affected by pore	-	-	Yes
E5	135	1.01	Yes, but also pore involved	-	-	Yes